9768–9778 *Nucleic Acids Research, 2011, Vol. 39, No. 22* *Published online 2 September 2011*
doi:10.1093/nar/gkr664

Influence of ground-state structure and Mg^{2+} binding on folding kinetics of the guanine-sensing riboswitch aptamer domain

Janina Buck[1], Anna Wacker[1], Eberhart Warkentin[2], Jens Wöhnert[3,*], Julia Wirmer-Bartoschek[1] and Harald Schwalbe[1,*]

[1]Institute for Organic Chemistry and Chemical Biology, [2]Max-Planck-Institute for Biophysics, Max-von-Laue-Strasse 1 and [3]Institute for Molecular Biosciences, Center for Biomolecular Magnetic Resonance, Johann Wolfgang Goethe-University, Max-von-Laue-Strasse 7 & 9, 60438 Frankfurt am Main, Germany

Received March 7, 2011; Revised July 26, 2011; Accepted July 28, 2011

ABSTRACT

Riboswitch RNAs fold into complex tertiary structures upon binding to their cognate ligand. Ligand recognition is accomplished by key residues in the binding pocket. In addition, it often crucially depends on the stability of peripheral structural elements. The ligand-bound complex of the guanine-sensing riboswitch from *Bacillus subtilis*, for example, is stabilized by extensive interactions between apical loop regions of the aptamer domain. Previously, we have shown that destabilization of this tertiary loop–loop interaction abrogates ligand binding of the G37A/C61U-mutant aptamer domain (Gsw^{loop}) in the absence of Mg^{2+}. However, if Mg^{2+} is available, ligand-binding capability is restored by a population shift of the ground-state RNA ensemble toward RNA conformations with pre-formed loop–loop interactions. Here, we characterize the striking influence of long-range tertiary structure on RNA folding kinetics and on ligand-bound complex structure, both by X-ray crystallography and time-resolved NMR. The X-ray structure of the ligand-bound complex reveals that the global architecture is almost identical to the wild-type aptamer domain. The population of ligand-binding competent conformations in the ground-state ensemble of Gsw^{loop} is tunable through variation of the Mg^{2+} concentration. We quantitatively describe the influence of distinct Mg^{2+} concentrations on ligand-induced folding trajectories both by equilibrium and time-resolved NMR spectroscopy at single-residue resolution.

INTRODUCTION

RNA function critically depends on RNA structure and folding; and both, RNA structure and folding can be significantly modulated by mono- and divalent cations (1–3). RNA folding kinetics are markedly influenced by the ground-state conformational RNA ensemble, and folding traps sequestering the folding-competent ensemble of functional RNAs are frequently encountered. The dependence of the rate of folding on the ground-state conformational ensemble is significantly more pronounced for RNA compared to proteins, since substantial barriers for inter-conversion exist between substates of RNAs with alternative base pairing schemes even if these substates can have almost identical stability (4).

Riboswitches, a class of *cis*-acting RNA regulatory elements, bind specific metabolites with high affinity and selectivity. Metabolite binding induces a substantial allosteric conformational rearrangement. Riboswitches, therefore, represent a particularly striking example for the coupling of ground-state conformational characteristics and the rate of productive ligand-induced RNA folding. The conformational switch is key to the RNA-based gene regulation mechanism and involves folding of the RNA into one of possible alternative structures (5,6). Ligand-binding changes long-range interactions in the complex riboswitch fold in response to local conformational changes. These conformational changes induced by ligand binding trigger signal transduction between different RNA domains.

For transcription-regulating riboswitches, several folding events and their rates are coupled to RNA-based regulation. Depending on ligand concentration, the rate of folding of the metabolite-sensing RNA aptamer domain, the ligand-binding event itself and the subsequently

*To whom correspondence should be addressed. Tel: +69 7982 9737; Fax: +69 7982 9515; Email: schwalbe@nmr.uni-frankfurt.de
Correspondence may also be addressed to Jens Wöhnert. Tel: +69 798 29271; Fax: +69 798 29527; Email: woehnert@bio.uni-frankfurt.de

The authors wish it to be known that, in their opinion, the first two authors should be regarded as joint First Authors.

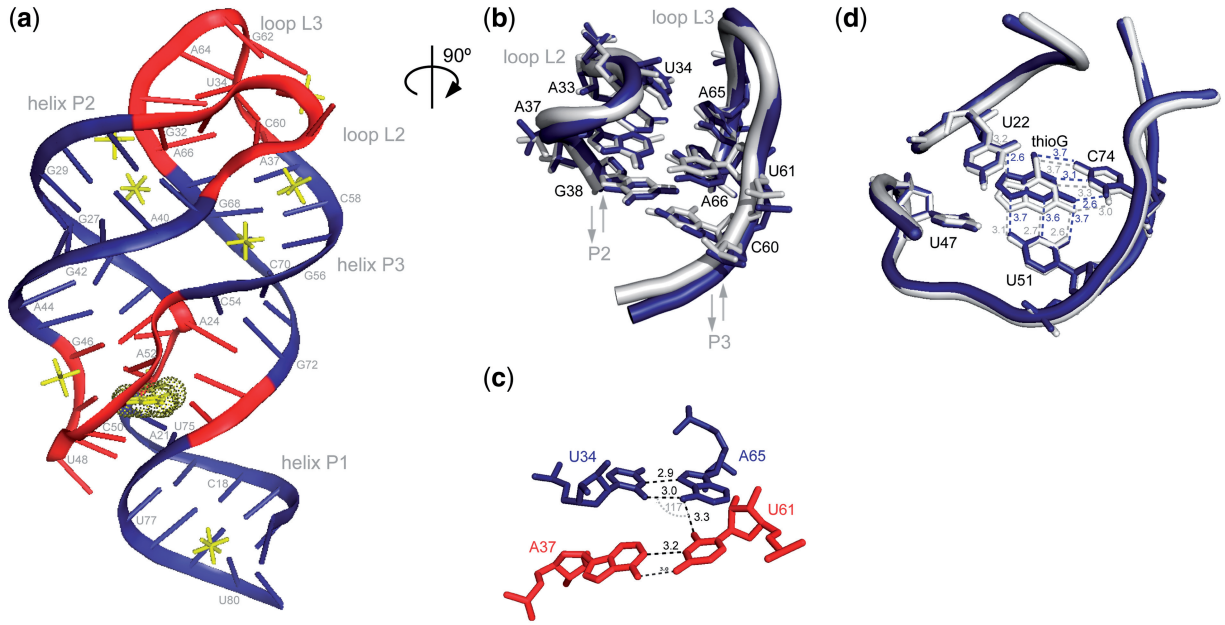

Figure 1. Crystal structure of the G37A/C61U-mutant (Gsw^{loop}) from the *B. subtilis* guanine-sensing riboswitch aptamer domain in complex with the ligand thioguanine (thioG); (**a**) ribbon representation of the 3D structure of the Gsw^{loop}–thioG complex (chain a). The ligand thioG is presented in yellow dots; helices P1, P2 and P3 are color coded in blue, ligand-binding core region and loop regions are color coded in red; cobalt hexamine ions are shown in yellow stick representation; (**b**) Close-up view (rotated by 90° along vertical axis) of tertiary loop–loop interactions (RNA backbone of residues 32–38 in L2 and 60–66 in L3 are given; gray: chain a, blue: chain b). Residues of inter-helical base quadruples are shown in stick representation (arrows indicate 5′- to 3′-helix direction); (**c**) stick representation of the inter-helical base quadruple, including the mutations; black dashed lines represent hydrogen bonds, mutated inter-base pair angle is annotated in gray [U34(O2)–A65(N6)–U61(O2) ∼117°]; (**d**) close-up view of ligand-binding region from crystal structure of Gsw^{loop}–thioG. Local heterogeneity can be observed in molecules of one asymmetric unit in agreement with NMR spectra (Supplementary Figure S2) (gray: chain a, blue: chain b, with respective atom distances annotated).

induced allosteric conformational rearrangement of the RNA regulatory structural element need to proceed in a time window suitable for interference with mRNA synthesis. Intrinsically coupled to the regulatory structural rearrangement is the ability of the aptamer domain to adopt a ligand-binding competent conformation. This ability constitutes a coupled pre-equilibrium to the regulatory conformational event.

Various X-ray structures of ligand-bound riboswitch aptamer domains illustrate a variety of different RNA molecular recognition motifs that achieve specific metabolite binding (7–9). Bivalent cations, in particular Mg^{2+}, often stabilize the 3D architecture of riboswitches and ligand binding can in fact even critically depend on them. In addition, X-ray and biochemical studies illustrate that the global architectures of a number of different riboswitch elements is stabilized by long-range tertiary RNA–RNA interactions. In numerous cases, these long-range tertiary interactions are relevant for riboswitch function and/or ligand binding (9). Thus, in addition to ligand concentration, structural organization of long-range tertiary elements in the aptamer domains and the Mg^{2+} dependence of their formation can affect the kinetics of ligand binding and further riboswitch regulation.

In order to correlate ground-state ensemble characteristics defined by highly conserved residues forming long-range interactions with RNA folding kinetics, we investigate here the structure of the G37A/C61U-mutant of the aptamer domain of the guanine-sensing riboswitch RNA from *Bacillus subtilis* by X-ray crystallography and static NMR spectroscopy. Additionally, we use time-resolved NMR spectroscopy to observe the ligand-induced folding kinetics and decipher how pre-formation and stabilization of structural elements affect the course of subsequent tertiary folding for guanine-sensing riboswitch aptamer domains.

In the ligand-bound form, the overall fold of the aptamer domain consists of three helical segments (P1–P3) (Figure 1 and Supplementary Figure S1) whose relative orientations are determined by a large number of tertiary interactions in the ligand-binding pocket as well as tertiary long-range loop–loop interactions (10,11). Stabilization of the loop–loop interaction leads to an almost parallel compact orientation of the two helices P2 and P3 that persist in the ligand-free state of the wild-type aptamer domain. As a result of the helical compactness, electrostatic repulsive interactions accumulate that need to be compensated by cations. The formation of the long-range loop–loop interactions sensitively depends on the sequence of interacting nucleotides and can therefore be disrupted even by conservative mutations. Previously, we could show by site-directed mutagenesis comparing the binding characteristics for the wild-type aptamer domain and a G37A/C61U-mutant that the stable formation of the loop–loop interaction is not a pre-requisite for specific ligand binding (12). The mutant Gsw^{loop} is substantially more dynamic; however, both long-range structure formation and ligand binding in

the core region can be restored and even induced independently as a function of the [RNA]:[Mg^{2+}] concentration ratio. Due to the possibility to resolve distinct conformational transitions by a combination of static and time-resolved NMR experiments, we are able to dissect ground-state conformational ensemble characteristics and relative contributions of different structural elements with the ligand-induced RNA folding rates. These variations of ground-state structural RNA ensemble characteristics yield insight in RNA structures and in their populations.

Thus, the mutant Gsw^{loop} represents an optimal system to determine how the 3D architecture of the guanine-sensing riboswitch is linked to its function and which processes determine the time scale of productive RNA folding and thus modulate transcriptional regulation. Next to structural modifications of ligand functional groups that were shown to be correlated with binding affinities (13), characterizing and potentially modulating the ligand-induced RNA folding processes is vital to understand this dynamic regulation processes and important for potential applications of these RNA modules.

MATERIALS AND METHODS

RNA synthesis

G37A/C61U-mutant aptamer domains of the guanine-sensing riboswitch of the *B. subtilis xpt-pbuX* operon were prepared by *in vitro* transcription as described before (12) (see Supplementary Data and Supplementary Figure S1 for RNA construct details). ^{15}N-labeled rNTPs were purchased from Silantes (Munich). NMR samples were prepared in H_2O/D_2O (9:1) using the following buffer conditions: 25 mM potassium phosphate, pH~6.2, 50 mM potassium chloride.

RNA crystallization and X-ray data collection

G37A/C61U-mutant RNA was concentrated to 450 µM in a buffer solution composed of 10 mM K^+–HEPES buffer (pH~7.5), 750 µM ligand thioguanine (thioG) and 5 mM $[Co(NH_3)_6]^{3+}$. Crystallization trials were performed using the hanging-drop vapor-diffusion method where 1 µl of the RNA solution was mixed with 1 µl of reservoir solution [5 mM K^+–HEPES (pH~7.5), 12 mM $[Co(NH_3)_6]^{3+}$, 25% polyethylene glycol 4000 and 450 mM ammonium acetate) and incubated at room temperature. RNA–thioG crystals grew within 1 day and were flash-frozen in liquid nitrogen after adding 30% 2-methyl-2,4-pentanediol for cryoprotection. Diffraction data at 2.5 Å resolution were collected at beamline PXII of the Swiss Light Source (Villigen, Switzerland). Data were processed using the XDS package (14). Unit-cell parameters are $a = b = 52.3$ Å, $c = 263.4$ Å and $\alpha = \beta = 90°$, $\gamma = 120°$.

X-ray structure determination and refinement

The X-ray structure was determined by molecular replacement with the program PHASER (15) using the structure of the *B. subtilis xpt-pbuX* guanine-sensing riboswitch RNA in complex with hypoxanthine [pdb code: 1U8D (10)] as the search model and assuming space group $P3_2$ (No. 145). Initial attempts using, for example, the apparent space group $P3_221$ had failed. Indeed tests for twinning [PHENIX (16) and the twinning server (17)] revealed nearly perfect merohedral twinning of the crystal (twinning fraction 0.466, twin-law –h,–k,l). The MR model was refined with PHENIX (16) and CNS (18) using non-crystallographic symmetry restraints and the twinning parameters. The R_{free}-factor was calculated using 5% of the data not used in the refinement. Manual model adjustment, mutation of residues and placement of thioG and of $[Co(NH_3)_6]^{3+}$ were carried out using COOT (19). In total 26 $[Co(NH_3)_6]^{3+}$ and 12 water molecules were identified on the basis of the electron density maps. The *R*- and R_{free}-factors for the final structure were 21% and 23%, respectively. X-ray data collection and refinement statistics are summarized in Supplementary Data and Supplementary Table S1. The RNA structures related by non-crystallographic symmetry are very similar. Therefore, the structure analysis is based on chain a. PyMol was used for calculating r.m.s.d. and for preparing figures. Structural analysis was performed using 3DNA (20).

NMR spectroscopy

NMR experiments were recorded on a Bruker NMR spectrometer AV700 MHz with a 5-mm *z*-axis gradient TXI-HCN cryogenic probe using a standard ^{1}H,^{15}N-HSQC pulse sequence at different temperatures (273–293 K) and ^{1}H,^{1}H-NOESY and ^{1}H,^{1}H{^{15}N-filter, ω_2}-NOESY pulse sequences (sample conditions: uniformly ^{15}N-labeled RNA and unlabeled ligand).

Time-resolved NMR spectroscopy

Kinetic NMR experiments were recorded on a AV700 MHz Bruker NMR spectrometer equipped with a 5-mm z-axis gradient TXI-HCN cryogenic probe at 283 K. The *in situ* initiation of the hypoxanthine- and/or Mg^{2+}-induced RNA folding processes was realized by using a rapid mixing device (21). Initially, a solution with a volume of 300 µl was placed in a NMR shigemi tube. The injection solution (cofactor) had a volume of 40 µl. The [RNA]:[ligand] ratios were ~1:1 and Mg^{2+} concentrations were specified in equivalents (eq) with reference to the respective final RNA concentration ($[RNA]_{abs}$~300–700 µM). The kinetic experiments were recorded with selectively ^{15}N-uridine-labeled RNA in conjunction with NMR filter experiments and analyzed as described, using the software TOPSPIN 1.3, felix2000 (MSI) and SigmaPlot 9.0 (22). Supplementary Figure S3 shows the appropriate nucleotide-specific NMR spectra of Gsw^{loop} prior to and after injection of the ligand hypoxanthine. Individual time constants of ligand-induced RNA folding were analyzed in time-resolved NMR experiments at an RNA concentration of $[Gsw^{loop}]$~670 µM and an [RNA]:[ligand]:[Mg^{2+}] ratio of ~1:1:8 with a time resolution of ~3.4 s/data point. The Mg^{2+} dependence of ligand-induced RNA folding of Gsw^{loop} was analyzed by determination of overall time

constants ($k_{overall}$ [s^{-1}]) for the individual kinetics at each [RNA]:[Mg^{2+}] ratio. The overall time constant $k_{overall}$ was calculated from the sum of normalized integrals over time of individual signals, respectively. The kinetic data were fitted with a monoexponential function, half-life values were obtained using the formula for a first-order process ($t_{1/2} = \ln 2/k$). The error, stated for k, is the fitting error. The error value for $t_{1/2}$ results from error propagation (Supplementary Data and Supplementary Table S2). Specifically, the result with the best accuracy could be obtained by integrating imino proton signals (40%) using all data points of the kinetics [as also performed for the wild-type RNA (22)]. For an analysis of the effects of different processing methods, we refer to Supplementary Table S3.

RESULTS

In order to dissect how pre-formation and stabilization of structural elements and conformational dynamics in the ligand-free state of the RNA ensemble affect the course of ligand-induced RNA folding and how compactness of RNA–ligand structure is linked to the energetic barriers of RNA refolding, we investigated the G37A/C61U-mutant (Gsw^{loop}) of the guanine-sensing riboswitch aptamer domain of the *B. subtilis xpt-pbuX* operon. RNA folding involves formation of hydrogen-bonding interactions in two structural regions of the aptamer domain: the long-range inter-helical structure and the ligand-binding core region. The mutations were designed in such a way that long-range interactions are weakened but can still form. However, in contrast to the wild-type guanine-sensing riboswitch aptamer domain, multivalent (bivalent) cations are crucial for ligand binding and different [RNA]:[Mg^{2+}] concentration regimes could be delineated which differ in the stabilization of long-range tertiary structure and in the ligand-binding characteristics for Gsw^{loop} (12). At intermediate [RNA]:[Mg^{2+}] concentrations, Gsw^{loop} binds hypoxanthine even without pre-formed loop–loop interaction, while at high [RNA]:[Mg^{2+}] concentrations, the loop–loop interaction is restored in the ligand-free RNA conformation (12).

Crystal structure of the G37A/C61U-mutant reveals a compact fold in the ligand-bound conformation

Crystals of the Gsw^{loop}–thioG complex belong to space group $P3_2$ and diffract up to 2.5 Å. The asymmetric unit contains four non-identical RNA chains (a–d) with each RNA chain bound to one thioG molecule. The four complexes per unit cell are pair-wise virtually identical, with r.m.s.d. of ~0.21 Å and ~0.22 Å between chain a and d and between chain b and c, respectively, and an r.m.s.d. of ~0.53 Å between chain a and chain b. A total of 26 $[Co(NH_3)_6]^{3+}$ ions were identified per asymmetric unit, with seven ions bound to chains a and d, respectively, five ions bound to chains b and c and two $[Co(NH_3)_6]^{3+}$ ions which cannot be specifically assigned.

Next to the smaller number of $[Co(NH_3)_6]^{3+}$-binding sites found for chains b and c, these two complexes display a slightly altered position of the ligand thioG in the binding pocket (Figure 1). The distance of the ligand Watson–Crick (WC)-site to the C74 WC site is reduced by ~0.2 Å (averaged over all three hydrogen bonds) compared to the complexes of chains a and d. In contrast, in chains b and c, the ligand sugar-edge distance to the U51 WC site is larger by ~0.9 Å, rendering hydrogen-bonding interactions between these nucleobases unlikely. Interestingly, this flexibility of the ligand position within the binding pocket is also observed by NMR spectroscopy (Supplementary Data and Supplementary Figure S2) and was previously proposed based on observations of ultrafast fluorescence spectroscopy. In this fluorescence study, alternative ligand positions were assigned to different possibilities of favorable stacking interactions in the sandwich-like binding pocket (23). Additionally, previous X-ray studies revealed a certain degree of flexibility by C74 upon binding to ligand analogs with modifications at their six-position (24). Due to the shift of thioG in the binding pocket of chain b versus chain a, the thioG-C74 interface is also affected and adopts a sheared conformation in the RNA chain b–thioG complex (Figure 1; Supplementary Data and Supplementary Figure S2). As the binding pocket structure of the complexes formed by RNA chains a and d represent the consensus ligand-bound form of the wild-type aptamer complex most closely (10,11), we will focus in the following on the structure of the RNA chain a–thioG complex.

The overall fold of the Gsw^{loop}–thioG complex is very similar to the wild-type aptamer domain bound to the ligand hypoxanthine (10) (r.m.s.d. ~0.85 Å) and purine-sensing riboswitches in general (11,25–27). All key secondary and tertiary structural features are maintained by the mutant aptamer domain, including the parallel arrangement of helices P2 and P3 that is stabilized by tertiary loop–loop interactions between L2 and L3 (Figure 1). Specifically, the long-range interactions are formed by residues G38 and A37 of loop L2 involved in WC base pairs with C60 and U61 of loop L3 and A33 and U34 of loop L2 forming non-canonical Hoogsteen base pairs to A66 and A65 of loop L3. Thus, introducing the conservative double mutation G37A/C61U results in the same loop–loop interaction architecture as in the wild-type, although local differences are observed in the crystal structure of the Gsw^{loop}–thioG complex. First of all, the backbone morphology of the loop–loop interaction as represented by the positions of the phosphorous atoms of residues 32–38, in L2, and residues 60–66, in L3, displays an r.m.s.d. of only ~0.6 Å to the corresponding wild-type sequence. The altered nucleotide sequence in the mutant results in formation of less inter- and intra-helical loop–loop hydrogen bonds. The WC base pair A37–U61 naturally has only two hydrogen bonds compared to three in case of the wild-type G37–C61 base pair. Furthermore, since the exocyclic amino group at position 2 of A37 is missing, a hydrogen bond to U34 cannot form. This lacking hydrogen bond leads to a different orientation of the Hoogsteen base pair U34–A65 with respect to base pair A37–U61 {inter-base pair angle [U34(O2)–A65(N6)–U61(O2)] ~117°} when compared to the wild-type, for which these base pairs are co-planar.

Interestingly, the double mutation induces mostly indirect effects in the context of the overall tertiary structure of the complex. The base quadruple containing the mutated base pair is mainly distorted at residues U34 and A65 versus the wild-type structure. The U34–A65 base pair is staggered by ~0.97 Å in the mutant, thereby weakening inter-base quadruple hydrogen bonding. This weakening is also observed by NMR spectroscopy in solution. The signal intensity of the U34 imino proton resonance is substantially decreased in the $^{1}H,^{15}N$-HSQC (12). The second base quadruple stabilizing the loop–loop interaction consists of the WC base pair G38–C60 and the Hoogsteen base pair A33–A66. Here, the WC base pair stacking below the mutated A37–U61 base pair is characterized by a significant propeller twist of ~−24° compared to ~−11° in the wild-type structure, while the Hoogsteen base pair is buckled by ~−18° versus ~−9° in the wild-type. Additionally, the double mutation leads to a reduced stability of the closing base pair A59–U67 of P3. The imino proton-mediated hydrogen bond distance is stretched by ~0.4 Å compared to the wild-type base pair, which is likewise observable by a weak signal intensity of imino proton signal U67 in the $^{1}H,^{15}N$-HSQC (12). In summary, the stability of the loop–loop interaction in the Gsw^{loop}–thioG complex is reduced by the loss of several hydrogen bonds and favorable stacking interactions relative to the wild-type, which is also reflected in thermal melting curves (12).

As a side remark, the crystal structure of the Gsw^{loop}–thioG complex also illustrates that the P2 stabilizing mutations introduced by us in NMR studies concerning the guanine-sensing riboswitch aptamer (12,22,28,29) has no influence on the tertiary fold of the final RNA–ligand complex as judged by a backbone r.m.s.d. of only ~0.61 Å compared to the wild-type sequence (Supplementary Figure S1).

Formation of ligand-binding functional states of Gsw^{loop}

The influence of Mg^{2+} on overall compaction of RNA and electrostatic compensation of negative charges has been shown for numerous RNAs. In agreement with previously observed Mg^{2+}-induced chemical shift perturbations (CSP) for several imino proton signals of (i) Gsw^{loop} and (ii) Gsw^{apt} by solution NMR (12,28), cobalt hexamine ions could also be identified in the crystal structure of the Gsw^{loop}–thioG complex as illustrated in Figure 2a. We compared the $[Co(NH_3)_6]^{3+}$-binding sites identified in the crystal structure to the RNA residues displaying significant NMR CSPs in Mg^{2+} titration experiments. (i) In comparison to NMR studies of Gsw^{loop}, all residues except for U26 and U34 that experience CSPs of ≥15 Hz in the Mg^{2+} titration experiments are also in close proximity to a bound $[Co(NH_3)_6]^{3+}$ ion in the crystal structure, supporting the role of $[Co(NH_3)_6]^{3+}$ as a Mg^{2+} outer-shell hydration mimic and likely excluding any essential role of inner-shell coordinated Mg^{2+}-ions for folding of this riboswitch RNA (Figure 2a). (ii) Comparison of the Gsw^{loop}–thioG crystal structure with both the wild-type crystal structure bound to hypoxanthine [pdb: 1U8D (10)] and Mg^{2+}-dependent NMR titration studies of Gsw^{apt} (28) revealed that exclusively G72 seems to be a unique Mg^{2+}-binding site for the wild-type RNA–ligand complex (Figure 2b). This imino proton shows no significant Mg^{2+}-induced CSPs by NMR in the mutant aptamer domain, while for all other residues, CSPs can be mapped to the same structural regions both in Gsw^{loop} (Figure 2a) and in Gsw^{apt} (Figure 2b).

As one example, we further characterized the effect of Mg^{2+} by inspection of NMR spectral characteristics of the imino proton signal of nucleotide U81 localized in helix P1, for which a cobalt hexamine ion could be observed in close spatial proximity within the crystal structure (Figure 2). At a $[Gsw^{loop}]:[Mg^{2+}]$ ratio of ~1:7, hypoxanthine binds to Gsw^{loop}; as a consequence of this binding process, the chemical shift of U81 changes by only $\Delta\delta$~8.2 Hz (Figure 2d). In contrast, Mg^{2+} binding to the RNA induces strong chemical shift changes of this signal. While a $[Gsw^{loop}]:[Mg^{2+}]$ ratio of ~1:7 induces a chemical shift change of $\Delta\delta_{(0-7eq)} \sim 24.6$ Hz, at a ratio of $[Gsw^{loop}]:[Mg^{2+}] \sim 1{:}20$ a difference of $\Delta\delta_{(0-20eq)}$~49.1 Hz is observed (Figure 2e). These NMR data illustrate that Mg^{2+} has a strong effect on the conformational ensemble characteristics of the free RNA, even before the RNA shows well-established long-range tertiary interactions (12). Time-resolved NMR experiments following spectral changes of the imino proton signal of nucleotide U81 over time reveal the kinetics of the respective Mg^{2+}-induced conformational changes of Gsw^{loop} to be faster than ~8–10 s (Figure 2c), in line with a rapid structural collapse induced by Mg^{2+} binding.

Ground-state conformational dynamics affect the time course of ligand-induced RNA folding

The mutant riboswitch Gsw^{loop} was designed to probe the importance of the long-range loop–loop interaction on ligand-induced folding rates and involved conformational states of the guanine-sensing riboswitch aptamer domain. Since pre-organization of the tertiary loop–loop interaction in the ligand-free state of Gsw^{loop} critically depends on the Mg^{2+} concentration, time-resolved NMR experiments of ligand-induced RNA folding were performed at various Mg^{2+} concentrations in order to investigate whether differences in the RNA folding rates can be observed (i) for different structural elements as previously detected for the wild-type Gsw^{apt} (12) and for other riboswitch aptamer domains, as e.g. the TPP-sensing riboswitch (30) and (ii) to test the influence of ground-state conformational dynamics on ligand-induced riboswitch folding.

Probing the impact of native tertiary structure pre-organization on ligand-induced RNA folding. We analyzed the ligand-induced RNA folding kinetics at a $[RNA]:[Mg^{2+}]$ ratio (~1:8), for which static NMR studies demonstrated ligand-binding competence but no stable pre-formation of long-range tertiary loop–loop interactions (12). Hypoxanthine-induced RNA folding could be monitored for 12 resolved imino proton reporter signals (Supplementary Data, Supplementary Figure S3 and Supplementary Table S2). Representative

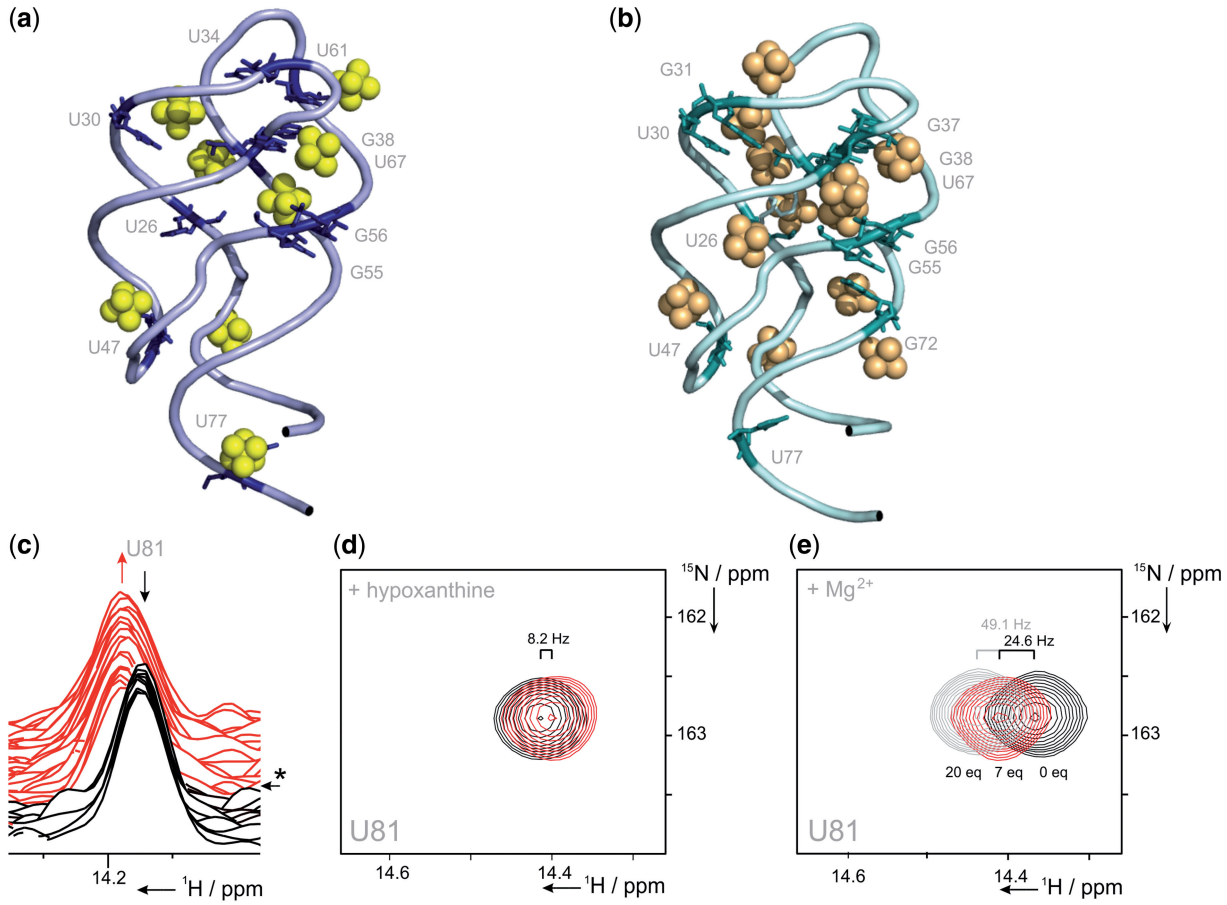

Figure 2. Hypoxanthine- and Mg^{2+}-induced effects on conformation and folding of Gsw^{loop}. (**a**) Mg^{2+} binding by the Gsw^{loop}–thioG complex (pdb: 3RKF). RNA residues of Gsw^{loop} (sequence position/structural element (77)/P1, (26, 30)/P2, (55, 56, 67)/P3), (34, 61, 38)/loop region, (47)/binding pocket that show NMR imino proton chemical shift changes upon Mg^{2+} titration $\Delta\delta_{(0-33eq)}>15$ Hz (12) are annotated in stick representation on the crystal structure of the G37A/C61U-mutant; cobalt hexamine ions are found in close proximity to the respective residues in the crystal structure (cobalt hexamine ions are highlighted in yellow); (**b**) Mg^{2+} binding by the Gsw^{apt}–hypoxanthine complex [pdb: 1U8D (10)]. RNA residues of Gsw^{apt} (sequence position/structural element (77)/P1, (26, 30, 31)/P2, (55, 56, 67, 72)/P3), (37, 38)/loop region, (47)/binding pocket that show NMR imino proton chemical shift changes upon Mg^{2+} titration $\Delta\delta_{(0-33eq)}>15$ Hz (28) are annotated in stick representation on the crystal structure of the wild-type Gsw^{apt}–hypoxanthine complex. Cobalt hexamine ions are found in close proximity to the respective residues in the crystal structure (cobalt hexamine ions are highlighted in orange); (**c**) kinetics of Mg^{2+}- and hypoxanthine-induced RNA–ligand complex formation. Spectral changes recorded for imino proton signal U81 over time [s] are illustrated (*): time point of injection ($t\sim0$ s) of Mg^{2+} and hypoxanthine; time resolution/1D spectrum ~8.6 s; black: 1D-spectra before injection, red: 1D-spectra following injection); (**d**) addition of hypoxanthine leads to small chemical shift changes of the imino proton signal of nucleotide U81 in helix P1 ($\Delta\delta\sim8.2$ Hz) (overlay of $^1H,^{15}N$-HSQC spectral region of U81/Gsw^{loop} at an [RNA]:[Mg^{2+}] ratio of ~1:7 in presence (red) and absence of hypoxanthine (black)); (**e**) addition of Mg^{2+} leads to significant chemical shift changes of U81 (overlay of $^1H,^{15}N$-HSQC spectral region at different [RNA]:[Mg^{2+}] ratios: $\Delta\delta_{(0-7eq)}\sim24.6$ Hz and $\Delta\delta_{(0-20eq)}\sim49.1$ Hz).

reporter signals could be determined for the ligand itself, the ligand-binding core region of the RNA, the helical elements as well as the tertiary loop–loop interactions. Kinetic analysis of the Gsw^{loop} folding process did not reveal significant differences in the folding kinetics of individual nucleotides for different structural elements (Figure 3 and Supplementary Table S2). The kinetic traces could be fitted to monoexponential functions and the determined half-lives ($t_{1/2}$ [s]) were found to vary between 20.1 s and 25.6 s (Supplementary Table S2). Destabilization of long-range tertiary structure of Gsw^{loop} and the consequently induced differences in ground-state conformational dynamics thus significantly alter the ligand-induced RNA folding process compared to the wild-type sequence (22).

Mg^{2+} dependence of the kinetic rates of ligand-induced RNA folding. We analyzed the Mg^{2+} dependence of the conformational ensemble characteristics of the ligand-free state of Gsw^{loop} on the kinetics of ligand-induced RNA folding by time-resolved NMR at [RNA]:[Mg^{2+}] ratios between 1:5 and 1:20. As kinetic rates did not show significant differences for individual nucleotides and could be fitted by monoexponential functions (Figure 3 and Supplementary Table S2), we determined an overall time constant $k_{overall}$ ([s^{-1}]) for ligand-induced RNA folding at each Mg^{2+} concentration. Supplementary Figure S4 shows the build-up kinetics at three characteristic [RNA]:[Mg^{2+}] ratios, indicating that ligand-induced RNA folding is strongly dependent on Mg^{2+} concentration.

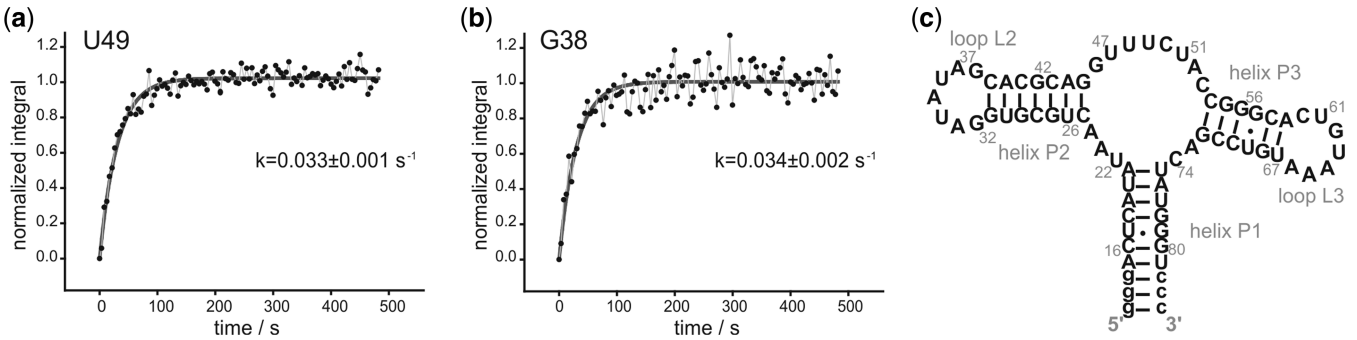

Figure 3. Ligand-induced folding of Gsw^{loop} ([RNA]:[ligand]:[Mg^{2+}] ~1:1:8, 700 MHz, 283 K). Normalized integrals over time [s] of exemplary imino proton signals of (**a**) nucleotide U49 within the ligand-binding core region and of (**b**) nucleotide G38 forming part of the long-range inter-helical base pairing interactions (dark gray solid line: monoexponential fit). (**c**) Secondary structure of the G37A/C61U-mutant of the guanine-sensing riboswitch aptamer domain of the *B. subtilis xpt-pbuX* operon (for further construct details, see Supplementary Data).

In addition to the influence of Mg^{2+} concentration on the kinetics of ligand-induced folding of Gsw^{loop}, we also observe that the populations of the ligand-free to the ligand-bound states at equimolar ratio of RNA and ligand are influenced by the Mg^{2+} concentration (Figure 4). Analysis of NMR spectra following ligand-induced RNA folding support that RNA–ligand complex formation is completed at [RNA]:[Mg^{2+}] ~ 1:20. At these experimental conditions, imino proton signals indicative for Gsw^{loop} in its free conformation can no longer be detected in the final ligand-bound state ([RNA]:[ligand]~1:1). In contrast, for [RNA]:[Mg^{2+}] ratios <1:20, NMR spectra show signals for the RNA–ligand complex as well as for the ligand-free conformation of Gsw^{loop} (Figure 4).

In conclusion, the fit of the rate-dependence $k_{overall}$ to a sigmoidal curve (Figure 5a) assumes that the dependence on the [Mg^{2+}]:[RNA] ratio approaches saturation at [Mg^{2+}]:[RNA] > 20:1. This is in agreement with the observation that at high [Mg^{2+}]:[RNA] ratios exclusively the ligand-bound state is populated (Figure 4).

Comparison of the Mg^{2+} influence on ground-state characteristics and kinetic rates of ligand-induced RNA folding for Gsw^{loop} and Gsw^{apt}. In contrast to the wild-type Gsw^{apt}, the mutant Gsw^{loop} RNA requires Mg^{2+} to rescue ligand-binding capability (12). Minor changes in the native RNA sequence result in fundamentally different folding behavior of the Gsw^{loop} RNA. Table 1 provides a comparison of structural characteristics and ligand-binding kinetics for Gsw^{apt} (22) and Gsw^{loop} for different relevant Mg^{2+} concentrations.

Structural characteristics of the ground-state ensembles are substantially affected by Mg^{2+} in case of the Gsw^{loop} RNA, however not as pronounced for the wild-type Gsw^{apt}. Ligand-induced folding of Gsw^{loop} at intermediate Mg^{2+} concentrations displays a smaller variance of nucleotide-specific kinetic rates compared to the wild-type. These individual kinetic variations are no longer correlated in context of the 3D structure (Supplementary Figure S5), consistent with a different folding pathway. Starting from a structurally less defined ensemble, due to only transiently stabilized tertiary interactions, the ligand-bound RNA is comparable to the wild-type complex. However, the presence of Mg^{2+} further induces electrostatic stabilization. Higher Mg^{2+} concentrations accelerate folding beyond time-scales accessible by real-time NMR (<10 s).

DISCUSSION

The restriction of the dynamic flexible conformational ensemble of the unfolded state of RNA toward the functional state is one of the major driving forces during RNA folding. The formation of a compact, partially structured intermediate state ensemble can restrict the number of dynamical accessible states and guide folding trajectories. Long-range tertiary contacts can determine folding rates and select for specific folding pathways (31,32). Due to the polyanionic character of RNA, electrostatic charge compensation represents a major barrier to be overcome when folding complex tertiary structures. Consequently, divalent cations are often essentially required to stabilize the functional RNA conformation as well as lowering energetic barriers of the RNA folding landscape.

For riboswitches as a recently identified class of RNA regulating elements, understanding the regulation mechanism and its dependence on ligand concentration and cofactor requirements is crucial to dissect the different factors that are important for the conformational rearrangement. By analyzing the effect of changing Mg^{2+} concentrations, we can delineate from other potential factors present in cells, including RNA chaperones, helicases and alike. The remarkable aspect of the free conformation of the guanine-sensing riboswitch aptamer domain in the absence of ligand and Mg^{2+} is the stably formed long-range loop–loop interaction, while nucleotides in the ligand-binding region are not involved in persistent base pairing interactions (28). Specific ligand binding can already be observed in the absence of Mg^{2+}. The addition of Mg^{2+} leads only to minor chemical shift changes of imino proton resonances indicating that Mg^{2+} does not significantly affect the ground state ensemble of the wild-type riboswitch. However, comparison of the relative stabilities of the RNA in the presence and absence of Mg^{2+} by temperature-dependent CD- and

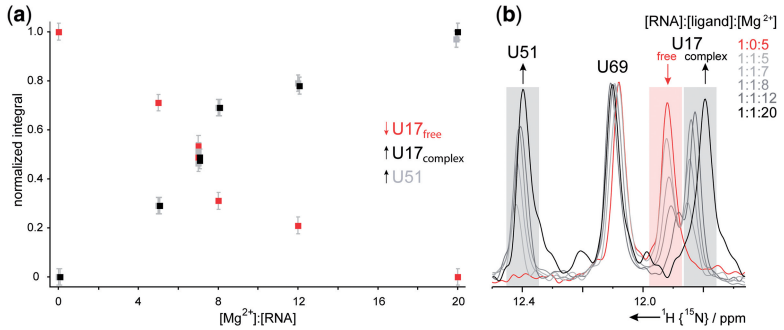

Figure 4. Dependence of the equilibrium of free Gsw^{loop} and Gsw^{loop}–hypoxanthine complex on Mg^{2+} concentration. Signals originating from nucleotide U51 can be detected only in the ligand-bound form, while signals from nucleotide U17 can be observed in the free ($U17_{free}$) and the RNA–ligand complex ($U17_{complex}$), however, with different chemical shifts. The signal of nucleotide U69 shows differences neither in intensity nor significantly in chemical shift in the two conformations. (**a**) Normalized integrals relative to the integral $U17_{total} = U17_{free} + U17_{complex}$ for imino proton signal of $U17_{free}$, $U17_{complex}$ and U51 as a function of the $[Mg^{2+}]$:[RNA] ratio. (**b**) Overlay of 1D NMR spectra (^{15}N-edited) of Gsw^{loop} (^{15}N-uridine labeled) in the presence of equimolar concentrations of hypoxanthine and varying concentrations of Mg^{2+} (signal-to-noise is normalized relative to signal of nucleotide U69).

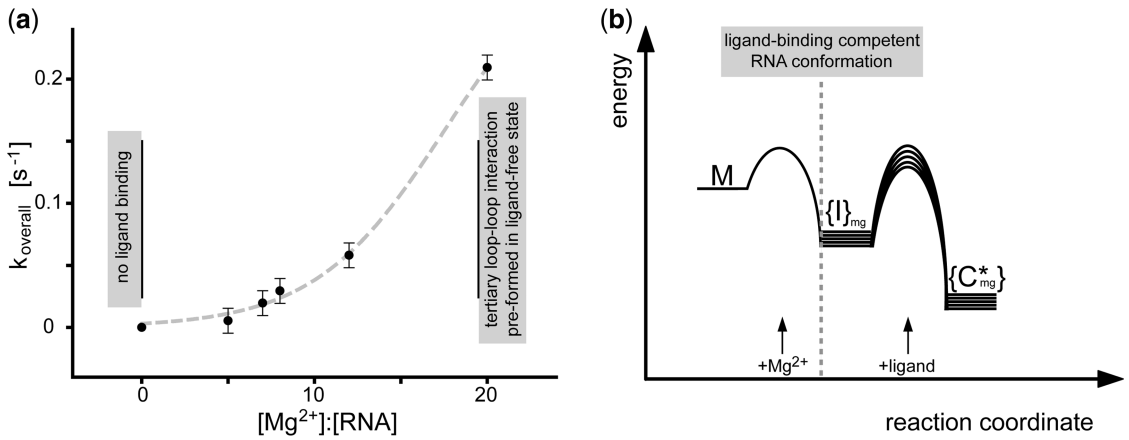

Figure 5. Mg^{2+} dependence of the ligand-induced Gsw^{loop} folding; (**a**) overall time constant $k_{overall}$ [s^{-1}] of ligand-induced RNA folding process as a function of $[Mg^{2+}]$:[RNA] ratio (the error is given from replica measurement at $[Mg^{2+}]$:[RNA] ~7:1; additional data at higher $[Mg^{2+}]$:[RNA] ratios >20:1 could not be obtained due to the limited time-resolution of the NMR measurements; gray dashed line: sigmoidal fit; the choice of the fitting function was motivated by assuming that $k_{overall}$ [s^{-1}] approaches saturation at an [RNA]:$[Mg^{2+}]$ ratio of 1:20); (**b**) free activation energies of the Mg^{2+}- and/or ligand-induced conformational transitions are schematically depicted. In the free G37A/C61U-mutant (M, absence of Mg^{2+}), secondary structure elements but neither the loop–loop interaction nor the ligand-binding region are pre-formed and Gsw^{loop} cannot bind ligand (28). Through variation of the [RNA]:$[Mg^{2+}]$ ratio, the ligand-binding capability can be restored ($\{I\}_{mg}$) as well as formation of the tertiary loop–loop interaction at high Mg^{2+} concentrations ([RNA]:$[Mg^{2+}]$ >1:18). In the schematic diagram, this observation leads to a conformational RNA ensemble, whose dynamic and structural properties are Mg^{2+} dependent (signified by {}). The addition of Mg^{2+} leads to a rapid RNA conformational change. The derivation is based on the experimental finding that the Mg^{2+}-induced conformational transition, monitored for Gsw^{loop} at an [RNA]:$[Mg^{2+}]$ ratio <1:18 ($M \rightarrow \{I\}_{mg}$), is faster than ~8–10 s. The conformational transitions induced by Mg^{2+} are very fast and associated with energetic barriers that are small compared to the barriers associated with ligand binding. The kinetics of ligand binding ($\{I\}_{mg} \rightarrow \{C^*\}_{mg}$) strongly dependent on the [RNA]:$[Mg^{2+}]$ ratio. The variation in kinetic rate constants from the $[Mg^{2+}]$ concentration implies Mg^{2+}-dependent differences of the free activation energy.

NMR experiments reveals significant stabilization, especially for the tertiary loop–loop interaction in the presence of Mg^{2+} but also for secondary structure (12).

Despite pronounced dynamics of the RNA ensemble in the ligand-free form of the G37A/C61U mutant studied here resulting from introduced mutations, the final complex state adopts a WT-like compact overall fold. Our crystal structure of the G37A/C61U-mutant RNA reveals a ligand-bound conformation for which the global architecture but also ligand recognition and formation of the binding pocket are almost identical to wild-type RNA–ligand complexes. The observed local structural differences in the tertiary loop–loop motif are in line with structural and stability differences compared to the wild-type guanine-sensing aptamer domain (12). The Mg^{2+} dependence of structure formation observed in NMR studies is confirmed by observation of cobalt hexamine ions in the crystal structure, supporting the need to balance electrostatic repulsion effects for RNA structure compactness.

Our observation of a fast Mg^{2+}-induced RNA folding process for Gsw^{loop} is in agreement with data for other RNAs (33). For the *Tetrahymena* ribozyme, Mg^{2+}-induced conformational changes appear at a time scale

Table 1. Comparison of RNA structural characteristics of Gsw^{apt} and Gsw^{loop} and kinetic data for ligand-induced folding obtained by time-resolved NMR; (T~283 K, ligand: hypoxanthine)

[a]Gsw^{apt} without Mg^{2+}	[a]Gsw^{apt} and Mg^{2+}	[b]Gsw^{loop} without Mg^{2+}	[b]Gsw^{loop} and Mg^{2+} (1:8)	[b]Gsw^{loop} and Mg^{2+} (1:33)
Ligand-binding competent	Ligand-binding competent	–	Ligand-binding competent	Ligand-binding competent
Loop–loop interaction preformed	Loop–loop interaction preformed	No tertiary structure	Tertiary structure transiently formed	Loop–loop interaction preformed
–	Electrostatic compensation by Mg^{2+}	–	Electrostatic compensation by Mg^{2+}	Electrostatic compensation by Mg^{2+}
Core signals, $t_{1/2}$~18.9–23.6 s	Folding completed <10 s	–	Core signals, $t_{1/2}$~20.1–25.6 s	folding completed <10 s
Loop/helix P2 signals, $t_{1/2}$~27.1–30.7 s	Folding completed <10 s	–	Loop/helix P2 signals, $t_{1/2}$~20.6–24.5 s	Folding completed <10 s

[a]Structural data published by Noeske *et al.* (28), kinetic data published by Buck *et al.* (22).
[b]Structural data published by Buck *et al.* (12).

of several milliseconds; these conformational changes have been interpreted as structural compaction and transient formation of native tertiary contacts (34–37). Persistently formed loop–loop interactions are not a pre-requisite for ligand binding but Mg^{2+} exerts additional conformational changes beyond the stabilization of tertiary native contacts. The conformational changes induced by Mg^{2+} are essential for formation of functional states but do, as observed, not represent rate-limiting steps for ligand binding and folding of Gsw^{loop}.

Comparison of kinetics at high Mg^{2+} concentration for Gsw^{apt} and Gsw^{loop} show that, once key tertiary structural motifs are formed, Mg^{2+} facilitates structural rearrangements and leads to fast RNA folding. This is in agreement with the observation that the RNA folding rate mainly depends on the stability of discrete folding intermediates (38). The sequential folding kinetics observed for the wild-type, Gsw^{apt} (22), are a result of hierarchical tertiary structure formation, which in turn depends on their respective stabilities. Once Mg^{2+} is present, such differences in stability are small compared to the large favorable electrostatic contributions offered by Mg^{2+} and such subtle effects are no longer observed in folding rate constants.

The differences in ligand-induced folding kinetics for individual nucleotides previously observed for the guanine-sensing riboswitch aptamer domain (22) (in the absence of Mg^{2+}) cannot be observed for Gsw^{loop} at an [RNA]:[Mg^{2+}] ratio of ~1:8. At this concentration ratio, the RNA is able to bind the ligand hypoxanthine despite the observation that the tertiary loop–loop interactions are not stably formed. Due to comparable time constants of all observed imino proton signals of Gsw^{loop}, we conclude that the underlying RNA folding processes proceed concerted and cooperative. For Gsw^{loop}, concurrent structuring of the ligand-binding core region and formation of the long-range tertiary loop–loop interaction directly leads to a folding trajectory resulting in a preferential compact orientation of the global RNA architecture. Under experimental conditions for which the tertiary loop–loop interactions are not pre-formed, kinetics of ligand binding strongly depend on the [RNA]:[Mg^{2+}] ratio. As shown in the schematic diagram in Figure 5b, this observation is assigned to a conformational RNA ensemble, whose dynamic and structural properties are Mg^{2+} dependent. The variation in kinetic rate constants from the Mg^{2+} concentration implies Mg^{2+}-dependent differences of the free activation energy (Figure 5b).

For Gsw^{loop}, the first Mg^{2+}-induced folding step is not strictly coupled to formation of the loop–loop interaction, but nevertheless leads to a ligand-binding competent RNA ensemble (12). This finding implies that Mg^{2+}-induced folding represents the first obligatory folding step of the RNA aptamer domain during *in vivo* transcription, initiated by free Mg^{2+}; its rate depends on the physiologically available Mg^{2+} concentration. The conformational dynamics of the RNA ensemble stabilized through Mg^{2+}-ions determine the rate of complex formation of the aptamer domain and the cognate ligand. These rates are markedly affected for Gsw^{loop}. The most compact structures and the fastest kinetics are detected in the presence of charge compensating counter ions. Mg^{2+} leads to electrostatic charge compensation or even the formation of long-range tertiary loop–loop interactions. For Gsw^{loop}, the tertiary loop–loop interactions form only at [RNA]:[Mg^{2+}] ratios >1:18, while at lower ratios the RNA ensemble is heterogeneous and the kinetics of folding are slow. A more heterogeneous RNA ensemble may lead to a strong entropic penalty in the ligand-induced folding, a factor that would increase the free activation energy of the folding reaction. The observed Mg^{2+} dependence suggests an important role for structural pre-organization of the free RNA ensemble to drive fast productive ligand-induced RNA folding.

Our time-resolved NMR kinetics of ligand-induced RNA folding reveal that the rate of the ligand-binding process is sensitively regulated by the exact sequence in remote structure elements not involved in ligand binding itself and by the Mg^{2+} concentration. The folding rate correlates with the degree of structural pre-organization and the stability of remote RNA–RNA interactions. These results are in line with our previous studies, showing the Mg^{2+} dependence of functional stability (12). The guanine-sensing aptamer mutant Gsw^{loop}, for which tertiary structure stabilization and the rate of ligand binding can be tuned through variation of the Mg^{2+} concentration might offer an interesting module for artificial riboswitch design in synthetic biology. The

biological function of the long-range loop–loop interaction might involve the suppression of alternative folding pathways. In a primordial scenario reminiscent of the 'RNA world', intramolecular RNA–RNA interactions might serve as a helper motif, a primitive intramolecular RNA chaperone, to ensure proper folding of the overall tertiary scaffold to promote local folding of the RNA and thereby enable ligand binding in a biologically relevant time window as ultimate regulatory trigger.

SUPPLEMENTARY DATA

Supplementary Data are available at NAR Online.

ACKNOWLEDGEMENTS

The authors thank Dr Ulrich Ermler, Ulrike Demmer, Elke Stirnal and Dr Christian Richter for excellent technical assistance.

FUNDING

Aventis foundation (to J.W.); DFG-supported "Cluster of Excellence: Macromolecular Complexes" membership (to H.S. and J.W.); DFG SPP: "Sensory RNA in prokaryotes" (to H.S.). Funding for open access charge: DFG.

Conflict of interest statement. None declared.

REFERENCES

1. Brion,P. and Westhof,E. (1997) Hierarchy and dynamics of RNA folding. *Annu. Rev. Biophys. Biomol. Struct.*, **26**, 113–137.
2. Draper,D.E., Grilley,D. and Soto,A.M. (2005) Ions and RNA folding. *Annu. Rev. Biophys. Biomol. Struct.*, **34**, 221–243.
3. Woodson,S.A. (2010) Compact intermediates in RNA folding. *Annu. Rev. Biophys.*, **39**, 61–77.
4. Thirumalai,D. and Hyeon,C. (2005) RNA and protein folding: common themes and variations. *Biochemistry*, **44**, 4957–4970.
5. Garst,A.D. and Batey,R.T. (2009) A switch in time: detailing the life of a riboswitch. *Biochim. Biophys. Acta*, **1789**, 584–591.
6. Winkler,W.C. and Breaker,R.R. (2003) Genetic control by metabolite-binding riboswitches. *Chembiochem*, **4**, 1024–1032.
7. Edwards,T.E., Klein,D.J. and Ferre-D'Amaré,A.R. (2007) Riboswitches: small-molecule recognition by gene regulatory RNAs. *Curr. Opin. Struct. Biol.*, **17**, 273–279.
8. Schwalbe,H., Buck,J., Fürtig,B., Noeske,J. and Wöhnert,J. (2007) Structures of RNA switches: insight into molecular recognition and tertiary structure. *Angew. Chem. Int. Ed. Engl.*, **46**, 1212–1219.
9. Serganov,A. (2009) The long and the short of riboswitches. *Curr. Opin. Struct. Biol.*, **19**, 251–259.
10. Batey,R.T., Gilbert,S.D. and Montange,R.K. (2004) Structure of a natural guanine-responsive riboswitch complexed with the metabolite hypoxanthine. *Nature*, **432**, 411–415.
11. Serganov,A., Yuan,Y.R., Pikovskaya,O., Polonskaia,A., Malinina,L., Phan,A.T., Hobartner,C., Micura,R., Breaker,R.R. and Patel,D.J. (2004) Structural basis for discriminative regulation of gene expression by adenine- and guanine-sensing mRNAs. *Chem. Biol.*, **11**, 1729–1741.
12. Buck,J., Noeske,J., Wöhnert,J. and Schwalbe,H. (2010) Dissecting the influence of Mg^{2+} on 3D architecture and ligand-binding of the guanine-sensing riboswitch aptamer domain. *Nucleic Acids Res.*, **38**, 4143–4153.
13. Kim,J.N., Blount,K.F., Puskarz,I., Lim,J., Link,K.H. and Breaker,R.R. (2009) Design and antimicrobial action of purine analogues that bind guanine riboswitches. *ACS Chem. Biol.*, **4**, 915–927.
14. Kabsch,W. (2010) XDS. *Acta Cryst.*, **D66**, 125–132.
15. McCoy,A., Grosse-Kunstleve,R., Adams,P., Winn,M., Storoni,L. and Read,R. (2007) Phaser crystallographic software. *J. Appl. Cryst.*, **40**, 658–674.
16. Adams,P.D., Afonine,P.V., Bunkoczi,G., Chen,V.B., Davis,I.W., Echols,N., Headd,J.J., Hung,L.W., Kapral,G.J., Grosse-Kunstleve,R.W. *et al.* (2010) PHENIX: a comprehensive Python-based system for macromolecular structure solution. *Acta Crystallogr. D Biol. Crystallogr.*, **66**, 213–221.
17. Yeates,T.O. (1997) Detecting and overcoming crystal twinning. *Methods Enzymol.*, **276**, 344–358.
18. Brunger,A.T. (2007) Version 1.2 of the crystallography and NMR system. *Nat. Protocols*, **2**, 2728–2733.
19. Emsley,P. and Cowtan,K. (2004) Coot: model-building tools for molecular graphics. *Acta Crystallogr. D Biol. Crystallogr.*, **60**, 2126–2132.
20. Lu,X.J. and Olson,W.K. (2003) 3DNA: a software package for the analysis, rebuilding and visualization of three-imensional nucleic acid structures. *Nucleic Acids Res.*, **31**, 5108–5121.
21. Mok,K.H., Nagashima,T., Day,I.J., Jones,J.A., Jones,C.J., Dobson,C.M. and Hore,P.J. (2003) Rapid sample-mixing technique for transient NMR and photo-CIDNP spectroscopy: applications to real-time protein folding. *J. Am. Chem. Soc.*, **125**, 12484–12492.
22. Buck,J., Fürtig,B., Noeske,J., Wöhnert,J. and Schwalbe,H. (2007) Time-resolved NMR methods resolving ligand-induced RNA folding at atomic resolution. *Proc. Natl Acad. Sci. USA*, **104**, 15699–15704.
23. Jain,N., Zhao,L., Liu,J.D. and Xia,T. (2010) Heterogeneity and dynamics of the ligand recognition mode in purine-sensing riboswitches. *Biochemistry*, **49**, 3703–3714.
24. Gilbert,S.D., Reyes,F.E., Edwards,A.L. and Batey,R.T. (2009) Adaptive ligand binding by the purine riboswitch in the recognition of guanine and adenine analogs. *Structure*, **17**, 857–868.
25. Edwards,A.L. and Batey,R.T. (2009) A structural basis for the recognition of 2′-deoxyguanosine by the purine riboswitch. *J. Mol. Biol.*, **385**, 938–948.
26. Kim,J.N. and Breaker,R.R. (2008) Purine sensing by riboswitches. *Biol. Cell*, **100**, 1–11.
27. Wacker,A., Buck,J., Mathieu,D., Richter,C., Wohnert,J. and Schwalbe,H. (2011) Structure and dynamics of the deoxyguanosine-sensing riboswitch studied by NMR-spectroscopy. *Nucleic Acids Res.*, Epub ahead of print May 16, 2011.
28. Noeske,J., Buck,J., Fürtig,B., Nasiri,H.R., Schwalbe,H. and Wöhnert,J. (2007) Interplay of 'induced fit' and preorganization in the ligand induced folding of the aptamer domain of the guanine binding riboswitch. *Nucleic Acids Res.*, **35**, 572–583.
29. Noeske,J., Richter,C., Grundl,M.A., Nasiri,H.R., Schwalbe,H. and Wöhnert,J. (2005) An intermolecular base triple as the basis of ligand specificity and affinity in the guanine- and adenine-sensing riboswitch RNAs. *Proc. Natl Acad. Sci. USA*, **102**, 1372–1377.
30. Lang,K., Rieder,R. and Micura,R. (2007) Ligand-induced folding of the thiM TPP riboswitch investigated by a structure-based fluorescence spectroscopic approach. *Nucleic Acids Res.*, **35**, 5370–5378.
31. Chauhan,S. and Woodson,S.A. (2008) Tertiary interactions determine the accuracy of RNA folding. *J. Am. Chem. Soc.*, **130**, 1296–1303.
32. Pan,J. and Woodson,S.A. (1999) The effect of long-range loop-loop interactions on folding of the Tetrahymena self-splicing RNA. *J. Mol. Biol.*, **294**, 955–965.
33. Thirumalai,D., Lee,N., Woodson,S.A. and Klimov,D. (2001) Early events in RNA folding. *Annu. Rev. Phys. Chem.*, **52**, 751–762.
34. Russell,R., Millett,I.S., Tate,M.W., Kwok,L.W., Nakatani,B., Gruner,S.M., Mochrie,S.G.J., Pande,V., Doniach,S., Herschlag,D.

et al. (2002) Rapid compaction during RNA folding. *Proc. Natl Acad. Sci. USA*, **99**, 4266–4271.
35. Das,R., Kwok,L.W., Millett,I.S., Bai,Y., Mills,T.T., Jacob,J., Maskel,G.S., Seifert,S., Mochrie,S.G.J., Thiyagarajan,P. *et al.* (2003) The fastest global events in RNA folding: electrostatic relaxation and tertiary collapse of the Tetrahymena ribozyme. *J. Mol. Biol.*, **332**, 311–319.
36. Kwok,L.W., Shcherbakova,I., Lamb,J.S., Park,H.Y., Andresen,K., Smith,H., Brenowitz,M. and Pollack,L. (2006) Concordant exploration of the kinetics of RNA folding from global and local perspectives. *J. Mol. Biol.*, **355**, 282–293.
37. Takamoto,K., Das,R., He,Q., Doniach,S., Brenowitz,M., Herschlag,D. and Chance,M.R. (2004) Principles of RNA compaction: insights from the equilibrium folding pathway of the P4-P6 RNA domain in monovalent cations. *J. Mol. Biol.*, **343**, 1195–1206.
38. Mitra,S., Laederach,A., Golden,B.L., Altman,R.B. and Brenowitz,M. (2011) RNA molecules with conserved catalytic cores but variable peripheries fold along unique energetically optimized pathways. *RNA*, **17**, 1589–1603.